



Mapping HI in the NGC 4636 Galaxy Group with FAST

Pei Zuo^{1,2}, Dong Yang^{1,3}, Jing Wang¹, Lister Staveley-Smith^{2,4}, Xuchen Lin^{1,3} , Bi-Qing For^{2,4}, Tobias Westmeier², Jie Wang⁵,
Kristine Spekkens⁶, Virginia Kilborn⁷, O. Ivy Wong^{2,4,8}, Di Li^{5,9}, Karen Lee-Waddell^{2,8}, Barbara Catinella^{2,4}, Luis C. Ho^{1,3},
Bärbel Koribalski^{10,11}, Bumhyun Lee¹² , and Ming Zhu⁵

¹ Kavli Institute for Astronomy and Astrophysics, Peking University, Beijing 100871, China; jwang_astro@pku.edu.cn

² International Centre for Radio Astronomy Research (ICRAR), University of Western Australia, Crawley, WA 6009, Australia

³ Department of Astronomy, School of Physics, Peking University, Beijing 100871, China

⁴ ARC Centre of Excellence for All Sky Astrophysics in 3 Dimensions (ASTRO 3D), Australia

⁵ National Astronomical Observatories, Chinese Academy of Sciences, Beijing 100101, China

⁶ Department of Physics and Space Science, Royal Military College of Canada, P.O. Box 17000, Station Forces, Kingston, Ontario, K7K 7B4, Canada

⁷ Centre for Astrophysics and Supercomputing, Swinburne University of Technology, John Street, Hawthorn, 3122, Australia

⁸ CSIRO Space and Astronomy, Australia Telescope National Facility, P.O. Box 1130, Bentley, WA 6102, Australia

⁹ Research Center for Intelligent Computing Platforms, Zhejiang Laboratory, Hangzhou 311100, China

¹⁰ CSIRO Space and Astronomy, Australia Telescope National Facility, P.O. Box 76, NSW 1710, Australia

¹¹ School of Science, Western Sydney University, Locked Bag 1797, Penrith, NSW 2751, Australia

¹² Korea Astronomy and Space Science Institute, Daejeon 34055, Republic of Korea

Received 2022 April 10; revised 2022 May 23; accepted 2022 June 10; published 2022 August 30

Abstract

This paper presents data from a 21 cm HI emission drift scan observation of a field partially covering the NGC 4636 galaxy group with the Five-hundred meter Aperture Radio Telescope (FAST). We construct a pipeline to reduce the data, and use SoFiA for source finding. When not contaminated by Radio Frequency Interference (RFI), the FAST observations are capable of detecting all of the galaxies previously detected by the Arecibo Legacy Fast ALFA (ALFALFA) survey in the same region. Comparing to ALFALFA for the detections in common, the FAST data show consistent integrated spectra when the HI disks are spatially unresolved, and capture more flux when the HI disks are resolved. The FAST data further reveal 10 new detections in the region mutually covered with ALFALFA, and 18 new detections beyond the footprint of ALFALFA. All of the new detections have the matching optical counterparts. For the member galaxies of the NGC 4636 group, the detection limit of FAST is deeper by 0.4 dex in HI mass than that of the ALFALFA data. After correcting for the incompleteness caused by RFI contamination, we show that the HI detection rate of galaxies rises steeply with radius out to the virial radius of the group, and flattens beyond that. We also examine four spatially resolved galaxy systems with potential tidal interaction features in detail. Considering that the data have been taken during the “shared-risk” period before a major source of local RFI was eliminated, the results highlight the power of FAST in detecting extragalactic HI.

Key words: Galaxy: evolution – atomic data – galaxies: groups: general

1. Introduction

The group environment is a major factor that regulates the evolution of galaxies. The galaxies in high local densities or more massive halos tend to be more gas poor, older and more bulge-dominated than the galaxies in lower densities and less massive halos (e.g., Blanton & Moustakas 2009). The trend is especially significant for low-mass ($\log M_*/M_\odot < 10.5$) and satellite galaxies (e.g., Brown et al. 2017; Cortese et al. 2021), which are considered to be the building blocks for more massive galaxies. This broad picture has been established through statistical analysis of global measurements, but the details of the underlying physical processes (e.g., tidal and ram pressure stripping) need to be better understood using deeper and better-resolved multi-wavelength observations of galaxies in a wide range of environments and redshifts. Of particular

relevance here are more detailed observations of HI in and around galaxies, as HI is the raw material for building galaxies, and environmental effects more strongly affect the low-surface density HI than other cold, baryonic components of galaxies.

The existing single-dish HI surveys are less than ideal for studying group environmental effects. General surveys like the Arecibo Legacy Fast ALFA survey (ALFALFA) (Giovanelli et al. 2005; Haynes et al. 2018), HI Parkes All Sky Survey (HIPASS) (Koribalski et al. 2004; Meyer et al. 2004), and the extended GALEX Arecibo SDSS Survey (xGASS) (Catinella et al. 2018) provide large samples, but are either shallow or selected by stellar mass, biasing against the population with low HI or stellar masses, which are most likely being affected by environments. The Group Evolution Multiwavelength Study (GEMS) (Kilborn et al. 2009) and the Arecibo Galaxy

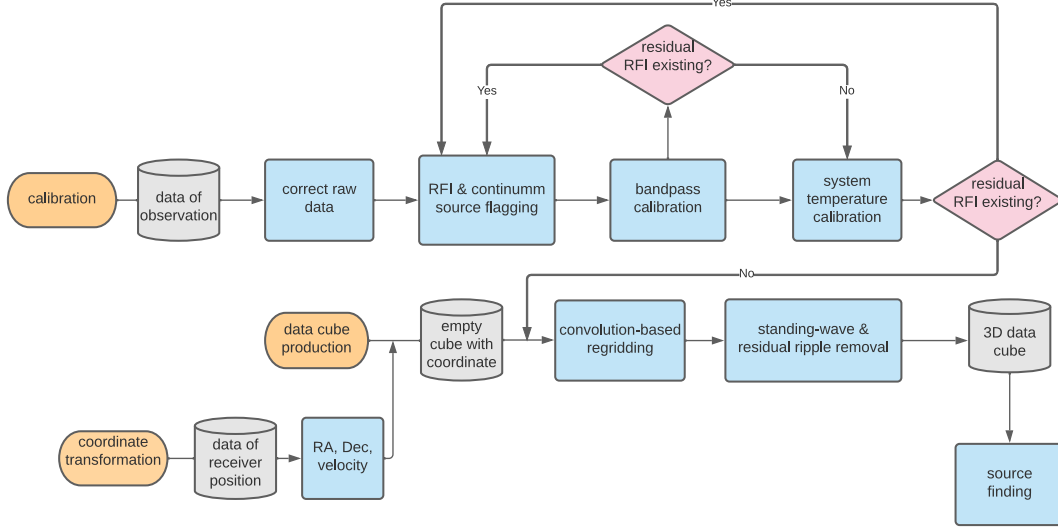


Figure 1. Flowchart outlining our data processing pipeline.

Environment Survey (AGES) (Auld et al. 2006) surveys mapped the HI in 16 and three local galaxy groups respectively. GEMS had a low angular resolution of $15'$, and a limiting HI mass sensitivity of only $\sim 10^8 M_\odot$. AGES reached a lower HI mass limit of $\sim 10^7 M_\odot$, but the small sample size makes it difficult to draw general conclusions.

The Five-hundred-meter Aperture Spherical Telescope (FAST) was fully constructed in 2016 and opened for “shared-risk” observations in 2019. A 19 beam receiver was installed in 2018 and its fundamental parameters, such as gain, pointing accuracy, aperture efficiency, and system temperature were found to meet design standard after a series of tests (Jiang et al. 2019, 2020). Jiang et al. (2020) confirmed that the stability and sensitivity of the 19 beam receiver is consistent with the expectations.

The high survey efficiency of FAST makes it possible to deeply map the HI with relatively high resolution in a statistically significant sample of local galaxy groups, which is the long-term plan of this project. One highlight of this project is the synergy with the Australian SKA Pathfinder (ASKAP) project, as part of the pilot survey for the Widefield ASKAP-band Legacy All-sky Blind survey (WALLABY) (Koribalski et al. 2020; T. Westmeier et al. 2022, in preparation). FAST has the advantage in detecting the large-scale diffuse HI and low-mass HI systems, while ASKAP can deblend the pairs/triples unresolved by FAST and resolve HI morphologies indicative of environmental effects. ASKAP has obtained HI images for several groups/clusters in the early science and pilot phases of WALLABY. For example, single dish observations of the IC 1459 group show that the ASKAP data missed 10% of the total HI mass in this group (Serra et al. 2015). The missing part is likely to be the diffuse intra-group gas. Combining interferometry and FAST, it is possible to capture

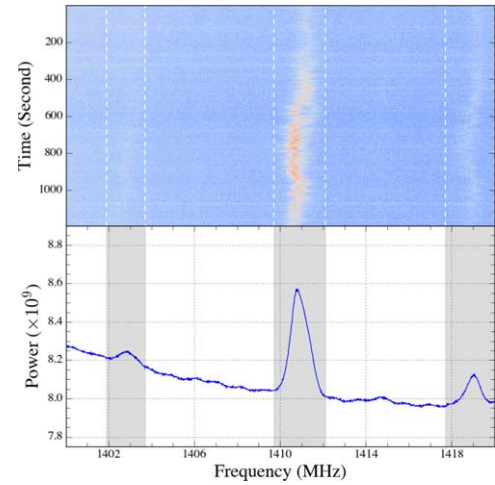


Figure 2. Example of three frequency bands of identified RFI with relatively persistent frequency ranges. The respective frequency ranges are 1401.5–1403.5, 1409.5–1412.0, and 1417.5–1409.0 MHz. Top: The waterfall image of one observational scan from one beam. The dashed white lines enclose the RFI region. Bottom: The median value of signal power along sampling time as a function of frequency for the above data. The gray shaded regions represent the RFI contaminated channels.

a more complete picture of the HI distribution in galaxy groups. We thus conduct a synergistic observing program with FAST and ASKAP, to map the HI in one group, NGC 4636. The group has a distance of 16.2 Mpc and a heliocentric velocity of 919 km s^{-1} , (Kourkchi & Tully 2017, Group 42 734) and is centered at $\alpha = 190^\circ 7084$, $\delta = 2^\circ 6880$. The X-ray analysis of the NGC 4636 group suggests a r_{200} of 0.61 Mpc (Reiprich & Böhringer 2002), from which a velocity dispersion of $\sigma_v = 278 \text{ km s}^{-1}$ can be deduced (Evrard et al. 2008). Here, r_{200} is the radius within which

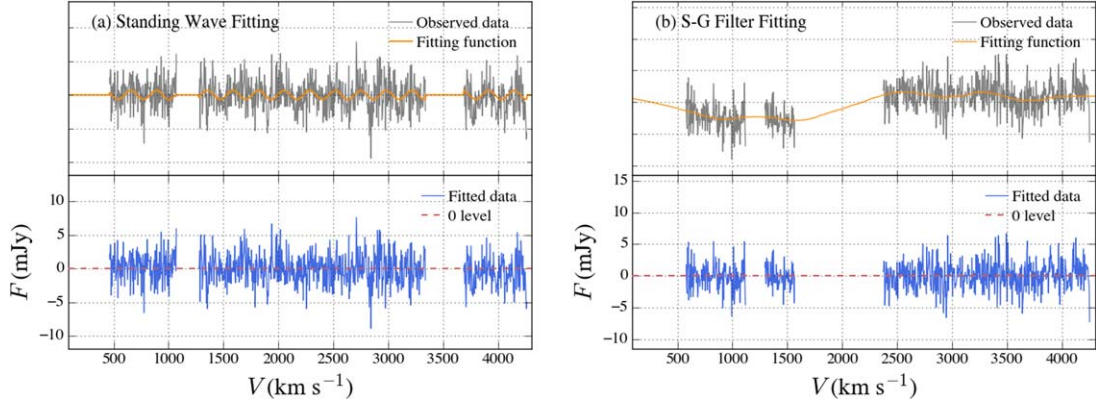


Figure 3. Examples of residual baseline fitting and subtraction. We show examples of a sine fitting (a) and an S-G filter fitting (b). In each example, (a) the spectral line before subtraction (gray) and the fitted line (orange); (b) the spectral line (blue) after subtracting the fitted residual, with the 0 level in red line. The blank part of the spectra represents the masked RFI.

the average density is 200 times the critical density of the universe. We take r_{200} as the virial radius r_{vir} .

Since the NGC 4636 group has an extended X-ray emitting halo (Baldi et al. 2009; Ahoranta et al. 2016), and the velocity dispersion of the group is $\sim 278 \text{ km s}^{-1}$, so both ram pressure and tidal stripping effects can be studied. ALFALFA detected 33 galaxies down to $M_{\text{HI}} = 2 \times 10^7 M_{\odot}$. Among all of the galaxies in the group, 34 of them have HI diameters $> 120''$ (based on the HI size-mass relation Wang et al. 2016), suitable for follow-up HI interferometric studies. The group lies close to the equator, suitable for performance tests of FAST at large zeniths, and suitable for synergistic observation with ASKAP.

In this paper, we present data taken with the FAST telescope. We describe the observations in Section 2. In Section 3, we introduce the procedure of reduction of FAST data. In Section 4, we present the basic HI data analysis of the NGC 4636 group. Section 5 investigates the HI detected population of the NGC 4636 group. Section 6 presents the resolved interacting candidate systems detected from the data. We summarize this work in Section 7. This work adopts the Lambda cold dark matter cosmology, with $\Omega_m = 0.3$, $\Omega_{\Lambda} = 0.7$, and $H_0 = 70 \text{ (km s}^{-1} \text{ Mpc}^{-1})$.

2. Observations

The data were acquired during a pilot cycle of “shared-risk” observations of FAST (PI: Wang; project code: 2019a-036-S), which were carried out using the 19 beam receiver at L band (1.05–1.45 GHz) in July and September 2019. To accomplish mapping of the NGC 4636 group, 14 decl. strips were designed to cover the $\sim 5^{\circ} \times 5^{\circ}$ region. Each strip required about 20 minutes to scan and the overhead time was ~ 12 minutes. The region was mapped twice and the total observation time is ~ 15 hr.

We conducted the observations in drift scan mode with a $23^{\circ}.4$ rotation angle of the receiver to achieve Nyquist sampling along the decl. direction. The sampling time is ~ 0.1 s and a 1 K noise diode was injected for calibration purposes during the observation. With 1,048,576 channels over a 500 MHz band, the original data stream was recorded with 0.475 kHz ($\sim 0.1 \text{ km s}^{-1}$) spectral resolution and dual polarization. In order to speed up the data processing described in Section 3, we rebin the velocity channels to $\sim 4 \text{ km s}^{-1}$ and constrain the frequency range to be 1400–1420 MHz, which is sufficient to cover the NGC 4636 group.

3. Data Reduction

The HI data were reduced using a custom Python script. The main procedures follow the standard steps of data processing for extragalactic HI drifting scans (e.g., HIPASS, Barnes et al. 2001 and ALFALFA, Haynes et al. 2018). The steps include radio frequency interference (RFI) flagging, calibration, regridding, and imaging. Besides the standard processes, we also developed methods to deal with a few specific problems, as the data being taken during the “shared-risk” stage of FAST when its performance was not optimal. These additional steps include correcting for noise injection issues, and flattening baselines caused by standing waves and RFI of local origin. The two polarizations are taken separately during all of the above procedures. The main processes of data reduction are illustrated in Figure 1 and explained below.

3.1. RFI Flagging

As with many radio observations, our data are contaminated with RFI, which need to be removed before an accurate calibration can be applied. Besides the effects from known satellites and GPS systems (1.15–1.21 GHz), extensive RFI of local origin was identified. Unlike the sporadic RFI, they have

relatively fixed central frequency and frequency width (Figure 2). The observed region also contains 26 continuum sources that are brighter than 0.1 Jy at 20 cm based on the NRAO VLA Sky Survey (NVSS) (Condon et al. 1998), but there can be weaker continuum sources not detected in NVSS. In order to obtain the HI data with optimized quality, we flag both RFI and potential continuum sources during the calibration.

We run the RFI flagging procedure twice in each round of data calibration processing, once before bandpass calibration and then again after scaling the data to units of temperature. This is because weak RFI is more obvious after the bandpasses are removed. The updated catalog of RFI flags is used for a new round of bandpass calibration. The cycle continues until no residual RFI is identified.

In each run of RFI flagging, we first use automated thresholds to flag the most obvious RFI, and then use an interactive interface to manually flag fainter suspected RFI. The procedure in each run of RFI flagging is similar to the MIRIAD task *pgflag*.

If a flagged baseline can be well fitted by a first order polynomial function, it is classified as a linear RFI, otherwise a nonlinear RFI. We mask both linear and nonlinear RFIs during calibration, but treat them differently during regridding and imaging. The linear RFI is treated like continuum spectra and subtracted, while the nonlinear RFI is masked.

3.2. Calibration

To calibrate the flux density scale, the 1 K signal of the noise diode was designed to inject into every other sample (one noise-on, one noise-off). Unfortunately, there was a synchronization mismatch between the sampling and the noise diode which led to loss of noise diode signal in the noise-on samples and leakage into the noise-off samples. As the mismatch was perfectly periodic, we were able to correct the data and reconstruct all spectral samples.

The flux calibration largely follows the standard procedure adopted by HIPASS and other surveys (Barnes et al. 2001; Haynes et al. 2011). The bandpass $\overline{P_{\text{off}}(t)}$ was obtained for each sampling point as the mean value of diode-off samplings over 90 s. For each sampling point, we calibrate the underlying bandpass against the noise diode, following the standard equation,

$$T_b(\nu) = \frac{\overline{P_{\text{off}}(t)}}{P_{\text{on}}(t) - P_{\text{off}}(t)} T_{\text{cal}}(\nu), \quad (1)$$

where T_b is the calibrated temperature of the observed data in K, $P_{\text{off}}(t)$ is the data with diode off, $P_{\text{on}}(t)$ is the data with diode on, and T_{cal} is the officially recorded temperature of the noise-diode in K, which needs to be interpolated in frequency as the channel resolution is 16 times coarser than the observed data.

The calculation of final flux density F requires division by the gain $G = G_0 \times \eta$, where G_0 is the perfect gain of the telescope and η is the aperture efficiency of the telescope. Based on Jiang et al. (2020), η linearly drops with zenith angle θ_{ZA} when it is larger than the angle of $26^\circ.4$, which corresponds to the upper limit of the illuminated aperture. Because the zenith angles of our observations are mostly $\geq 26^\circ.4$, we take the η for each of the 19 beams respectively from Jiang et al. (2020). Then the η dependent gain is factored into the calibration and the derived data are finally in units of Jy.

3.3. Imaging

The telescope pointing coordinates for each sample are converted into Equatorial sky coordinates. The velocity is converted to the heliocentric system.

We follow the convolution-based technique in Winkel et al. (2016) to grid the samplings into a data cube in terms of the coordinates. The main procedures are (1) construct a data cube with basic information in the header file and empty data array, (2) assign the samples from the calibrated data pool into the related pixels according to the coordinates, (3) calculate the weighting function of samples depends on the beam size and the distance from the pixel center, and (4) obtain the value of each pixel by calculating the weighted sum of the corresponding samples. The principal algorithm is expressed as

$$F = \sum_{i=0}^N (F'_i \times w_i), \quad (2)$$

where F is the estimated flux density of each pixel, F'_i is the flux density from each surrounding sample, w_i is the weighting of the related samplings, and N is the number of the samples. The weighting function is a Gaussian with full width at half maximum (FWHM) determined by the beam size,

$$w_i = \exp\left(\frac{-(\delta\alpha_i^2 + \delta\beta_i^2)}{2\sigma_{\text{kernel}}^2}\right), \quad (3)$$

where $\delta\alpha_i$ and $\delta\beta_i$ are the distances between the coordinates of sampling i and the pixel center. We choose $\sigma_{\text{kernel}} = \sigma_{\text{beam}}/2$ as suggested by Winkel et al. (2016), where σ_{beam} can be derived from the FWHM of the FAST beam ($2'.9$). The w_i equals to 0 when it is greater than $3\sigma_{\text{kernel}}$. Finally, the size of the final data cube is $420 \times 460 \times 1048$ (R.A. \times decl. \times Velocity) and the pixel size is $\sim 0'.6$, which is roughly one-fifth of the FAST beam size.

3.4. Continuum and Residual Baseline Subtraction

The spectra of galaxies in the cube have continuum which needs to be subtracted before the emission line can be analyzed. We subtract all continuum-like baselines before producing scientific products. This is done by fitting 2nd order polynomial functions to the spectral baselines after masking significant emission line like features.

Table 1
Catalog of Galaxies with Clean H I Spectra in NGC 4636 FAST Observation

No.	ID	UGC/NGC ID	SDSS ID	R.A. ($^{\circ}$)	Decl. ($^{\circ}$)	$V_{\text{H I}}$ (km s^{-1})	$F_{\text{H I}}$ (Jy km s^{-1})	S/N	$\log M_{\text{H I}}$ (M_{\odot})	Flag	Code
(1)	(2)	(3)	(4)	(5)	(6)	(7)	(8)	(9)	(10)	(11)	(12)
1	J123020+034418	UGC 7644	J123020.70+034424.5	187.5825	3.7382	4142	4.99 ± 0.03	151.0	9.62	2	2, 3
2	J123016+030403	...	J123016.28+030422.4	187.5687	3.0675	4046	0.74 ± 0.02	31.3	8.77	...	2, 3
3	J123803+001019	...	J123802.96+001037.4	189.5134	0.1719	3973	1.13 ± 0.02	74.8	8.94	...	2, 3
4	J123806-000136	UGC 7800	J123805.33-000137.3	189.5245	-0.0266	3707	5.64 ± 0.03	212.3	9.58	...	2, 3
5	J123630+001331	...	J123630.61+001319.0	189.1273	0.2253	3681	6.49 ± 0.02	343.1	9.63	...	2, 3
6	J124258-011234	UGC 7883	J124257.26-011345.9	190.7399	-1.2095	3163	14.38 ± 0.03	554.0	9.85	2	1, 3
7	J123613-010133	...	J123613.28-010136.5	189.0553	-1.0258	2506	1.84 ± 0.02	109.6	8.76	...	1
8	J123652-003523	...	J123651.88-003515.8	189.2186	-0.5897	2546	0.41 ± 0.01	38.5	8.11	...	1, 3
9	J123404+014610	...	J123402.08+014555.6	188.5150	1.7695	2464	1.78 ± 0.02	102.7	8.72	...	2, 3
10	J123417+034402	...	J123417.32+034420.6	188.5694	3.7338	2413	0.30 ± 0.01	31.7	7.93	...	2, 3
11	J124010-002114	...	J124008.73-002104.8	190.0401	-0.3538	1696	1.21 ± 0.01	93.7	8.23	...	1, 3
12	J123322+013128	...	J123320.76+013117.7	188.3428	1.5244	1670	2.10 ± 0.02	93.1	8.45	...	2, 3
13	J124003-010257	...	J124002.92-010302.9	190.0117	-1.0493	1591	1.57 ± 0.02	94.4	8.29	...	1, 3
14	J123228+002321	NGC 4517A	J123227.94+002326.2	188.1160	0.3893	1522	49.28 ± 0.04	1393.6	9.74	1	2, 3
15	J123248+013410	...	J123246.59+013408.1	188.1983	1.5695	1522	1.31 ± 0.01	97.7	8.17	...	2, 3
16	J124139+015027	...	J124139.20+015016.3	190.4131	1.8407	1526	0.59 ± 0.01	46.8	7.82	...	2, 3
17	J123643+030628	UGC 7780	J123642.07+030630.3	189.1772	3.1078	1438	8.35 ± 0.03	297.7	8.92	...	2, 3
18	J124320+015834	NGC 4643	J124320.13+015841.7	190.8327	1.9760	1310	1.26 ± 0.02	61.3	7.89	...	2, 3, *
19	J122939+033658	...	J122939.11+033645.6	187.4116	3.6161	1335	0.95 ± 0.02	54.7	7.91	...	2, 3, *
20	J123245+000645	NGC 4517	J123245.34+000648.8	188.1869	0.1124	1129	155.97 ± 0.04	3777.2	9.98	...	2, 3, *
21	J123950+014020	UGC 7824	J123950.60+014023.9	189.9590	1.6722	1222	3.18 ± 0.02	151.6	8.29	...	2, 3, *
22	J124428+002817	UGC 7911	J124428.77+002804.9	191.1182	0.4714	1180	16.41 ± 0.03	610.9	9.01	...	2, 3, *
23	J123537+030155	NGC 4544	J123536.57+030204.3	188.9059	3.0319	1148	3.25 ± 0.03	106.0	8.30	...	2, 3, *
24	J122904+000604	...	J122903.25+000616.9	187.2662	0.1012	1199	0.83 ± 0.01	81.74	7.71	...	2, 3, *
25	J123643-002524	189.1789	-0.4234	1150	0.22 ± 0.01	35.63	7.13	...	1, 3, *
26	J123355+033256	UGC 7715	J123355.71+033244.8	188.4815	3.5489	1135	2.27 ± 0.02	139.36	8.15	...	2, 3, *
27	J123104+014030	...	J123103.49+014032.2	187.7646	1.6750	1103	2.73 ± 0.02	170.24	8.23	...	2, 3, *
28	J124228+010550	...	J124228.58+010551.5	190.6177	1.0972	962	0.52 ± 0.01	38.33	7.51	...	2, 3, *
29	J124323+032525	...	J124321.05+032512.9	190.8472	3.4237	953	0.24 ± 0.01	20.62	7.18	...	2, 3, *
30	J123329+034729	...	J123329.57+034738.1	188.3727	3.7915	909	1.14 ± 0.02	69.40	7.85	...	2, 3, *
31	J124324+012447	190.8504	1.4130	932	0.18 ± 0.01	26.73	7.06	...	1, 3, *
32	J122857+034630	...	J122859.08+034647.6	187.2371	3.7750	825	0.21 ± 0.01	15.56	7.11	...	1, 3, *
33	J123256+032145	...	J123254.94+032146.3	188.2334	3.3625	739	0.97 ± 0.02	58.64	7.78	...	2, 3
34	J123309-003210	...	J123307.94-003158.9	188.2875	-0.5360	725	2.60 ± 0.02	166.78	8.20	...	2, 3, *
35	J123657+013632	...	J123654.95+013654.2	189.2372	1.6089	583	1.43 ± 0.02	65.23	7.95	...	2, 3, *
36	J122959+000133	...	J122958.84+000138.0	187.4950	0.0259	2410	0.44 ± 0.01	32.82	8.10	...	2, 3
37	J123358+002320	...	J123358.60+002313.0	188.4931	0.3890	1561	0.12 ± 0.01	12.23	7.16	...	1, 3
38	J123145+002159	187.9376	0.3663	1710	0.07 ± 0.01	13.64	7.00	...	1
39	J124034+004646	...	J124035.22+004611.2	190.1421	0.7794	1568	0.20 ± 0.01	16.27	7.38	...	2, 3
40	J123655+010903	189.2294	1.1508	1569	0.25 ± 0.01	18.71	7.47	...	1
41	J124028-005023	...	J124027.67-005023.5	190.1149	-0.8396	3400	0.74 ± 0.01	55.54	8.62	...	1
42	J124113-004501	...	J124112.41-004524.5	190.3044	-0.7504	3360	0.99 ± 0.01	80.50	8.74	...	1, 3
43_1	J124350-003341	NGC 4653	J124350.90-003340.4	190.9586	-0.5613	2613	32.79 ± 0.04	928.50	10.038	...	1, 3
43_2	J124318-003832	NGC 4642	J124317.75-003839.4	190.8247	-0.6421	2631	8.55 ± 0.03	290.37	9.46	...	2, 3
44_1	J123702+004750	189.2600	0.7972	2575	0.17 ± 0.01	23.92	7.74	...	1
44_2	J123657+004209	...	J123655.98+004125.0	189.2371	0.7026	2530	0.75 ± 0.02	39.55	8.37	...	2, 3

Table 1
(Continued)

No.	ID	UGC/NGC ID	SDSS ID	R.A.	Decl.	V_{HI}	F_{HI}	S/N	$\log M_{\text{HI}}$	Flag	Code
(1)	(2)	(3)	(4)	($^{\circ}$)	($^{\circ}$)	(km s^{-1})	(Jy km s^{-1})	(9)	(M_{\odot})	(11)	(12)
45	J124232-000520	NGC 4632	J124232.52-000458.1	190.6353	-0.0888	1712	57.41 ± 0.02	...	9.912	...	2, 3
46	J124228+000248	...	J124227.74+000253.5	190.6161	0.0468	1535	0.24 ± 0.01	32.23	7.44	...	1, 3
47_1	J124112+012423	...	J124111.57+012437.0	190.3018	1.4064	1685	10.58 ± 0.02	430.72	9.16	...	2, 3
47_2	J124119+013250	190.3286	1.5473	1677	0.50 ± 0.01	61.55	7.83	...	2, 3
48	J122902+024316	UGC 7612	J122902.17+024323.8	187.2585	2.7212	1567	14.81 ± 0.03	531.80	9.25	...	2, 3
49	J123013+023729	UGC 7642	J123013.38+023730.5	187.5555	2.6247	1628	5.01 ± 0.02	316.84	8.81	...	2, 3
50_1	J124508-002750	NGC 4666	J124508.60-002742.8	191.2825	-0.4639	1529	106.44 ± 0.04	2338.73	10.08	...	2, 3
50_2	J124532-003203	NGC 4668	J124531.99-003208.5	191.3820	-0.5343	1614	18.91 ± 0.02	899.51	9.38	...	1
50_3	J124548-002554	...	J124547.92-002556.6	191.4482	-0.4316	1668	0.77 ± 0.01	94.07	8.02	...	1
51_1	J123918-003155	NGC 4592	J123918.73-003155.0	189.8236	-0.5320	1072	245.12 ± 0.05	4932.03	10.13	...	2, 3, *
51_2	J123903-003951	189.7607	-0.6642	1140	1.53 ± 0.01	133.24	7.98	...	1, 3, *
52	J122856+033400	NGC 4457	J122859.03+033414.2	187.2344	3.5667	889	4.74 ± 0.03	163.13	8.40	3	2, 3, *
53	J124645+025947	...	J124649.55+030028.9	191.6860	2.9965	1233	1.58 ± 0.02	67.14	7.67	3	2, 3, *
54	J124018-001102	...	J124018.17-001106.3	190.0741	-0.1840	3722	0.50 ± 0.01	38.65	8.53	...	1
55	J123903+005112	...	J123902.48+005058.9	189.7645	0.8534	1593	0.11 ± 0.01	12.59	7.13	...	1
56	J124049+002648	...	J124048.46+002655.5	190.2051	0.4468	1721	0.13 ± 0.01	11.51	7.27	...	1
57	J123929+001707	...	J123929.36+001706.6	189.8723	0.2854	3016	0.37 ± 0.02	19.52	8.22	...	1
58	J123005-002449	...	J123002.09-002438.0	187.5224	-0.4136	2455	0.32 ± 0.02	20.10	7.97	...	1
59	J123727+013924	...	J123726.61+013941.4	189.3623	1.6568	1407	0.23 ± 0.01	21.43	7.34	...	2

Notes.

(1) No., cataloged number of source finding. The numbers with underscores indicate the sources which belong to the interacting candidate systems.

(2) ID, ID of FAST observation derived from the coordinates.

(3) UGC/NGC ID.

(4) SDSS ID.

(5), (6) Equatorial coordinates in degrees (J2000).

(7) H I velocity.

(8) Total integrated flux of H I line.

(9) S/N of the profile, obtained from SoFiA results.

(10) H I mass.

(11) Flag: 1 = confused, where the H I source has one more optical object within the beam. 2 = not fully covered by mapped region, FAST beam or the bandpass. 3 = within 3 beam FWHM to the edge of mapped region whose flux calibration may be wrong.

(12) Code: 1 = newly detected source by FAST. 2 = detected source by FAST and previous H I surveys. 3 = detected source have optical counterpart. * = detected source within the NGC 4636 galaxy group.

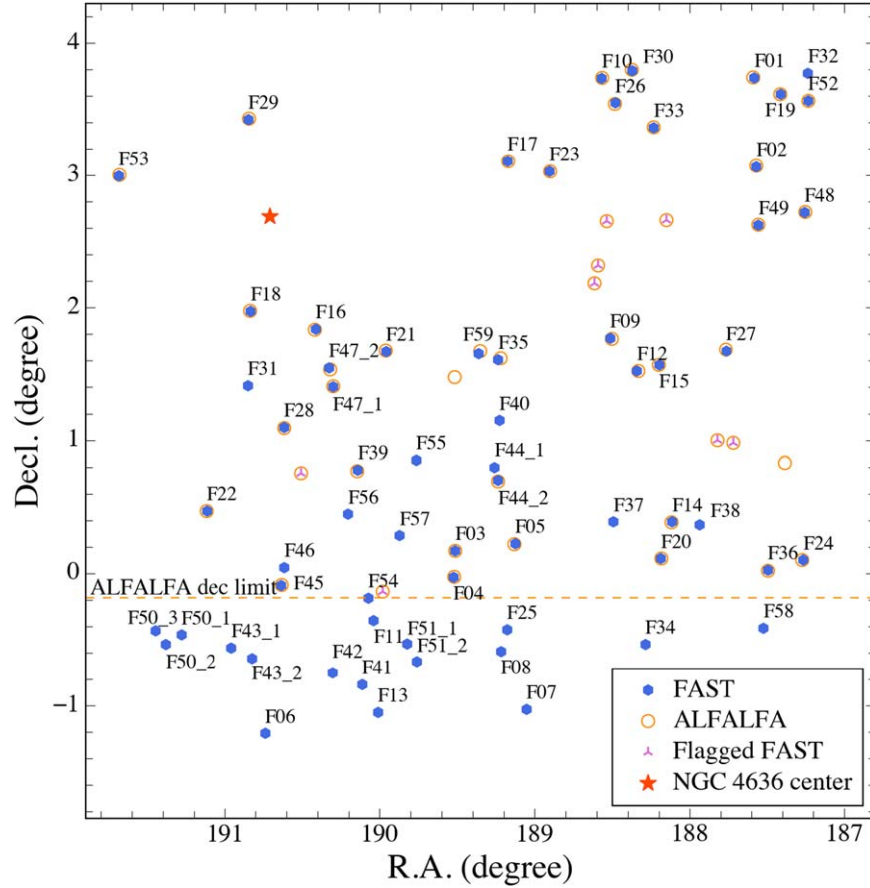


Figure 4. The sky distribution of FAST and ALFALFA detected sources in the observed region. The red star marks the center of the NGC 4636 group. The ALFALFA footprint only covers the northern sky above the orange line in the figure. The sources detected by FAST and ALFALFA are plotted as blue hexagons and orange circles respectively. The RFI contaminated and thus partly detected ALFALFA sources are shown with purple inverted “Y”.

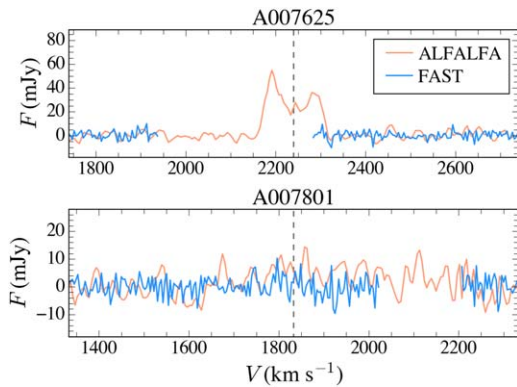


Figure 5. Spectra of the two galaxies that are detected by ALFALFA but not by FAST. In each panel, the central velocity (gray dashed line) of the H I line is in the middle of the displayed velocity range. The blue spectra are from the FAST observation, where the blank regions are contaminated by RFI. The orange spectra are from ALFALFA. The upper source totally lies in RFI contaminated region of the FAST data, and the bottom galaxy is a decode = 2 in ALFALFA.

The spectra of the data cube after continuum subtraction have residuals, though the bandpass has been removed during flux calibration and the continuum has been subtracted. There are mainly two types of baseline residuals (Figure 3). One type is pseudo-periodic with a wavelength of approximately 1 MHz, which is commonly associated with standing waves. We use the sine function to fit and subtract this. The other type is an irregular ripple or jump in the baseline of unknown origin. These irregular residuals are mostly found in beams M02 and M08, and increase the rms of the related spectra by $\sim 40\%$. To minimize this effect, we use a Savitzky–Golay (S-G) filter to obtain the underlying residual continuum.

4. Data Analysis

4.1. Source Catalog

The source finding was carried out in two rounds. The first round is by visual inspection, and the second round is based on an optical catalog with redshift measurements. In the first

round, three people independently visually inspect each data cube, and mark candidates. We require each candidate to have continuous extension of at least 3 pixels in all three-dimensions. We take the overlap from the three independent searches as the final catalog of detected galaxies in this round. In the second round, an early version of an optical catalog of galaxies from X. Lin et al. (2022, in preparation) (galaxies with available redshifts) is used as input for the *optfind* script of the software SoFiA (Serra et al. 2015; Westmeier et al. 2021). SoFiA searches for H I fluxes around the input coordinates, and returns detections. The ratio of the integrated flux of a source and its measured statistical uncertainty is referred to as signal-to-noise ratio (S/N), which obtained is by SoFiA (Westmeier et al. 2021).

In total, we detected 65 sources with H I emissions in the observed region (Table 1), and 12 of them are not included in the initial input optical catalog. We update the optical catalog of Lin et al. (2022, in preparation) with these 12 newly detected sources. In both rounds, we run SoFiA again around the coordinates of these 65 sources, to produce source masks, moment maps, and a catalog of flux properties. The cataloged properties include the flux weighted central coordinate, total flux, signal to noise ratio, and line width of each source.

The H I mass calculation is based on the expression of $M_{\text{HI}} = 2.36 \times 10^5 D^2 (S\Delta V) M_{\odot}$, where D is the luminosity distance in Mpc for the galaxies which do not belong to the group and is 16.2 Mpc for the group galaxies, $S\Delta V$ is the velocity-integrated H I flux density in Jy km s^{-1} . We list them in Table 1.

4.2. Comparison with ALFALFA

We compare our H I data to those from ALFALFA in the overlapping sky region, to quantify the data quality. Figure 4 shows the sky distribution of sources detected by FAST and ALFALFA. We detect all of the ALFALFA detected galaxies except for two. We have checked at the location of the two sources that are detected by ALFALFA but not by FAST in the data cube and extracted the spectra within $6\frac{1}{5}$ around them, which are shown in Figure 5. One of the two sources is located in a RFI-contaminated region, while the other one is barely detected by ALFALFA (code = 2 in Haynes et al. 2018). Of the 45 galaxies both detected by ALFALFA and FAST, 8 are partly contaminated by RFI in the FAST data, one target is at the edge of the velocity range. The remaining 36 sources are uncontaminated galaxies. Besides F39 (code = 2), the others belong to code = 1 in the ALFALFA catalog. These sources will be used as the comparison sample later.

In addition, there are 10 newly detected sources by FAST in the mutually-covered sky area with ALFALFA thanks to its higher sensitivity and smaller beam size. Figure 6 shows the relation between decl. and integral fluxes of all the FAST detections. 6 out of the 10 new detections have the integral

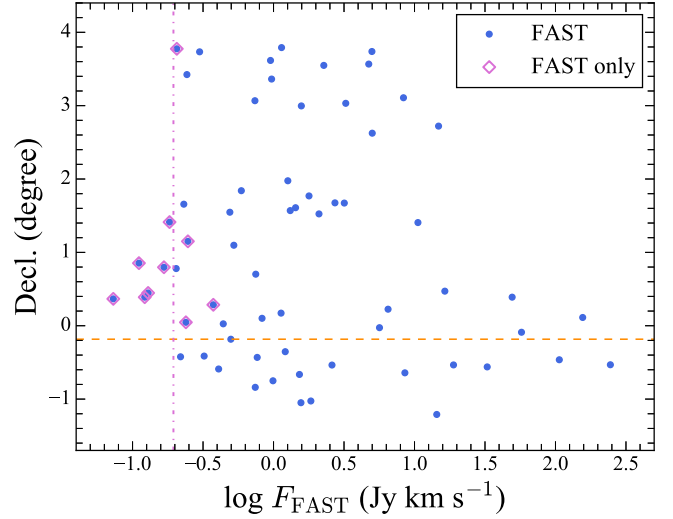


Figure 6. The relation between decl. and integral fluxes for FAST detections. The blue points represent FAST detections in this paper. The points enclosed with a purple diamond are the sources only detected by FAST. The orange dashed line is southern edge of the ALFALFA footprint, similar to that in Figure 4. The purple dashed-dotted line indicates an integral flux of $0.19 \text{ Jy km s}^{-1}$.

fluxes which are lower than $\sim 0.19 \text{ Jy km s}^{-1}$ and no ALFALFA sources in this region were reported below this value. And there are 18 sources detected by FAST below the celestial equator as ALFALFA only covers the northern sky with a limited decl. angle ($\sim 0^\circ$ – 36° , orange line in Figures 4 and 6), and 4 of them had been detected by HIPASS. Thus in total our FAST observations detect 24 new sources (Figure 7).

The total flux in galaxies detected by FAST has been calculated using SoFiA. The source mask generated by SoFiA for each galaxy covers all pixels containing detectable flux, making it possible to derive accurate flux of extended sources. In case flux from extended sources was missed in the ALFALFA catalog (Haynes et al. 2018), we thus compare the FAST data with the ALFALFA data depending on the typical size of sources. We use the H I size-mass relation (Wang et al. 2016) to estimate the characteristic size of the H I disk, R_{HI} , which is the radius where the surface density reaches $1 M_{\odot} \text{ pc}^{-2}$. We refer to the galaxies with R_{HI} larger than the beam FWHM of FAST as the resolved sources. The majority of the detected galaxies are not resolved, with $R_{\text{HI}} < \text{FWHM}$.

In Figure 8, we can see that for the unresolved sources, besides those fluxes are lower than $\sim 1 \text{ Jy km s}^{-1}$, the fluxes from FAST match well with those from ALFALFA. While for the resolved sources, the fluxes from FAST are higher than those from ALFALFA, which can be caused by the existing missing flux in ALFALFA catalog. The pipeline algorithm they used for producing catalog may miss flux from the very extended or highly asymmetric sources (Haynes et al. 2018;

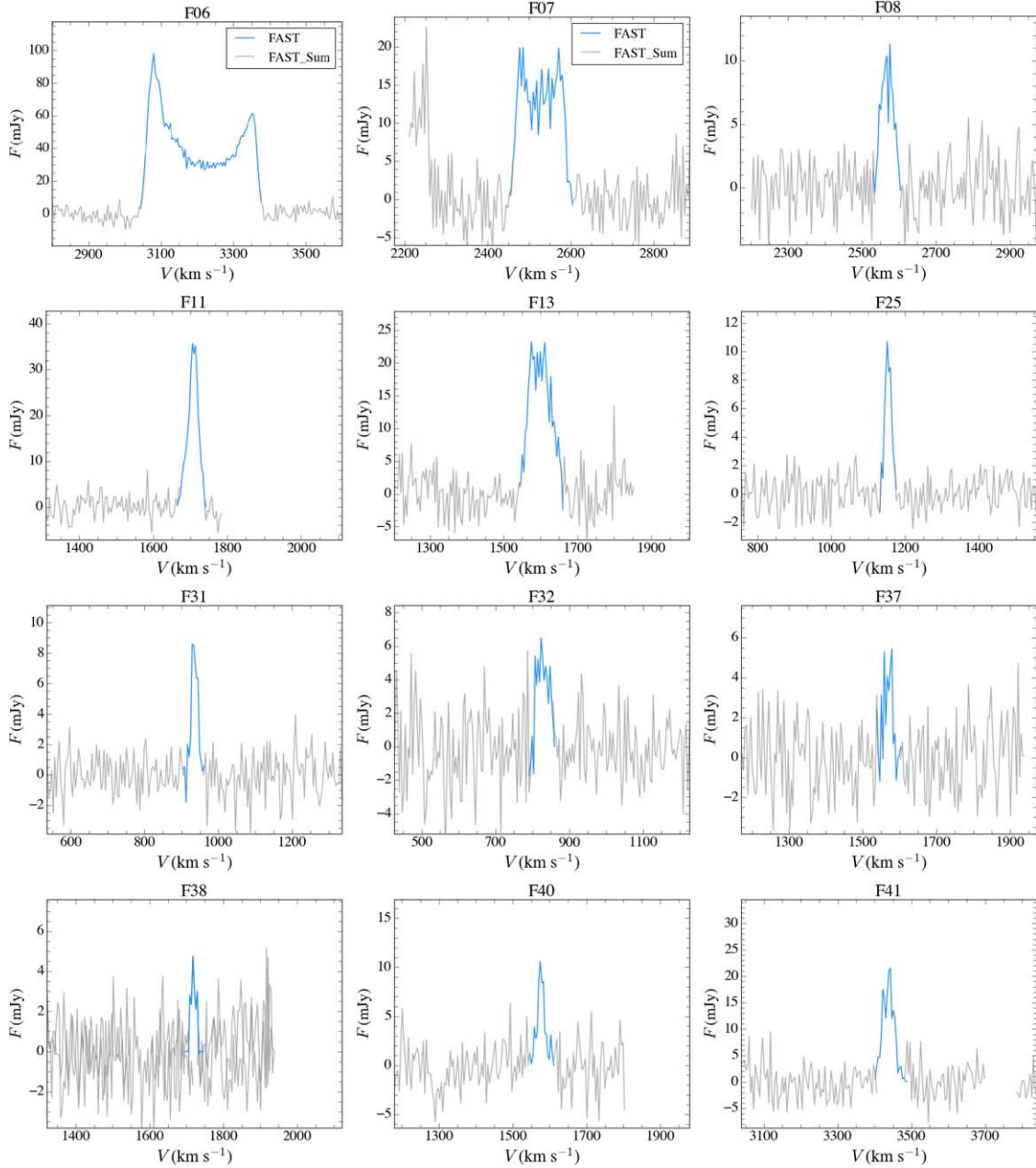


Figure 7. The H I spectra for newly detected sources in the FAST observations. The spectra in blue show the detected lines obtained by SoFiA. The spectra in gray show the noise level of the integral baseline along the line of sight of the detected region by FAST. The blank regions in the gray spectra are regions contaminated by the RFI.

Hoffman et al. 2019). Thus, the H I mass of these sources are higher than those in ALFALFA catalog.

The conclusion is strengthened by the comparison in spectral shapes between FAST, ALFALFA, and HIPASS. In Figure 9, for the unresolved sources, most of the spectra from FAST share similar shapes and amplitudes to the data from ALFALFA, confirming the good data quality from FAST. Note that the FAST spectra of two sources (F52 and F53) may

have uncertain flux calibration as they are near the edge of the observing footprint (2.0 and 2.2 beamwidths respectively). There are a few other sources (e.g., F05, F10, F17, F36, F47_1, and F59) for which the spectra from the two surveys do not well match in shapes or amplitudes. We have checked the distribution of these sources on the sky and found that they are located randomly in different strips and beams, which means the discrepancy is not due to different beam shapes or gain

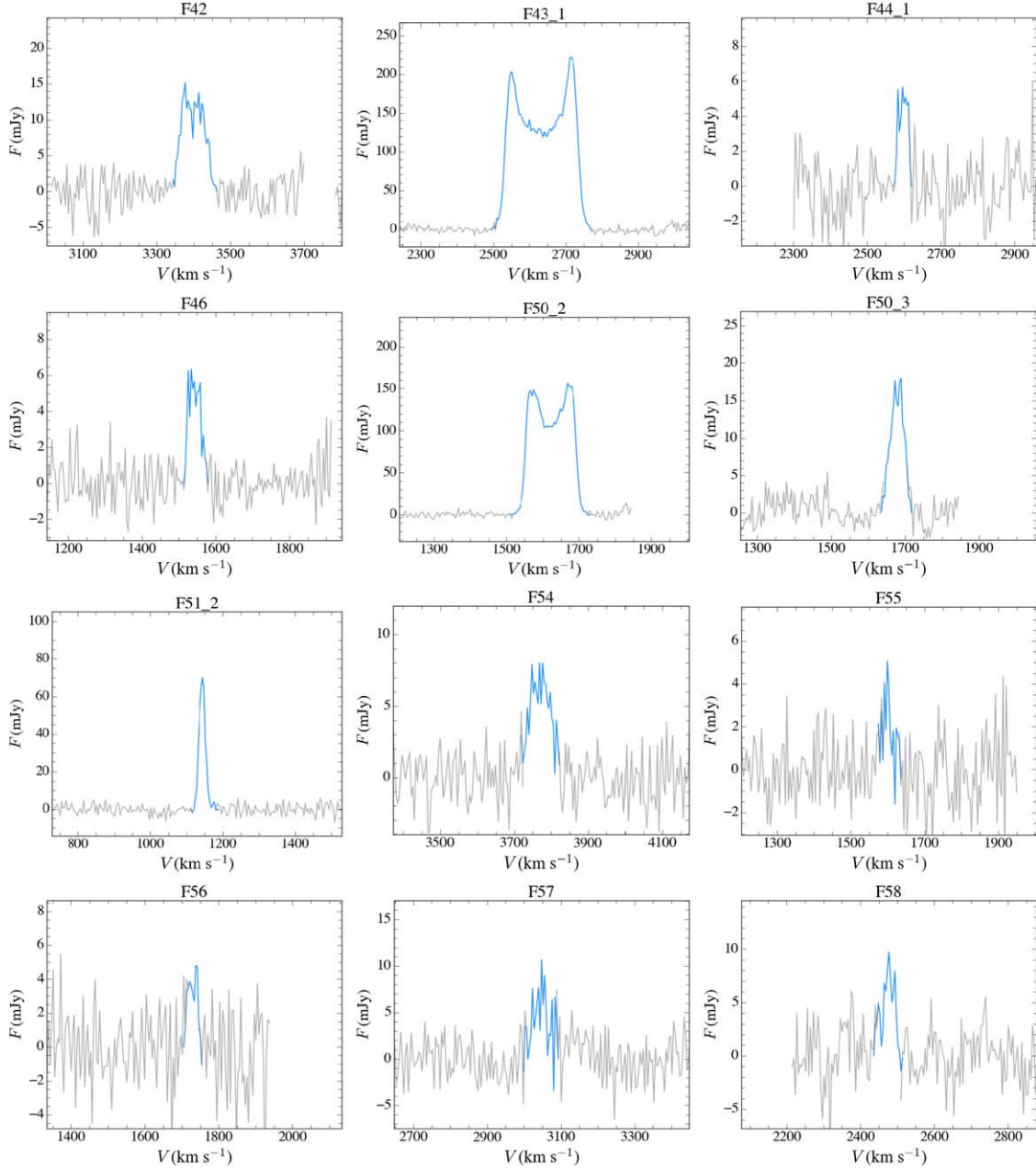


Figure 7. (Continued.)

values. However, as shown in Figure 8, the integral fluxes even for these sources typically differs by less than 25%. For the resolved sources in Figure 10, the FAST fluxes are clearly higher than those from ALFALFA, which shows the potential of FAST scans in capturing the total HI content for local extended sources.

Considering the data has been taken during the “shared-risk” period, the result from these tests highlights the power of FAST in detecting extragalactic HI.

5. The HI Detected Population of NGC 4636 Group

In this paper we focus on the region observed by FAST in the NGC 4636 group. A full analysis of the whole NGC 4636 group combining FAST with ASKAP and ALFALFA data, including regions not covered by the FAST footprint, will be presented in Lin et al. (2022, in preparation). We take the optical sample and related measurements from Lin et al. (2022, in preparation), including optical magnitude and stellar mass.

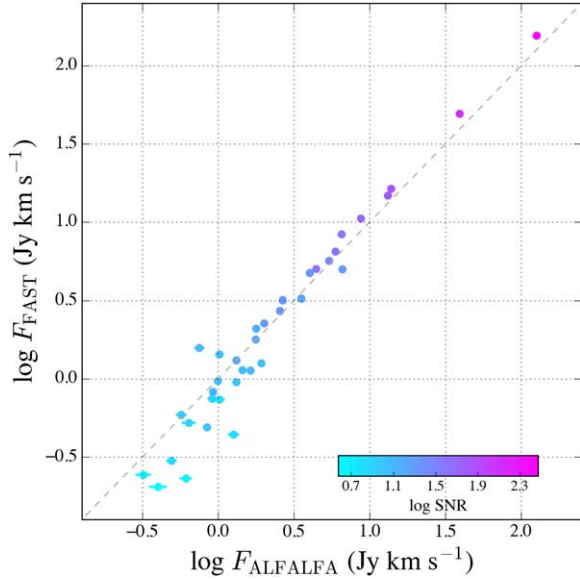


Figure 8. The comparison of integral fluxes between FAST and ALFALFA data. The colorbar represents the S/N in a log scale. The right most five points are resolved sources, and we expect the FAST fluxes to be more complete and thus higher than the ALFALFA fluxes. Most error bars are too small to show clearly.

We refer to Lin et al. (2022, in preparation) for more details but describe briefly the measurements below.

Lin et al. (2022, in preparation) start with all unique galaxies with redshift measurements from SDSS DR16 SpecObj table, galaxy catalog by Kourkchi & Tully (2017), ALFALFA (Haynes et al. 2018), HIPASS BGC (Koribalski et al. 2004), GEMS (Kilborn et al. 2009). They then select group members by requiring the radial velocity offset from the group center to be less than the escape velocity, and the projected group centric distance to be less than twice the virial radius r_{vir} . We further select the member galaxies in the sky region covered by this FAST observation, and update the sample with the nine newly detected (thus redshift available) galaxies. Because all of these galaxies with redshifts have optical counterparts, we refer to them as the group sample. This is the parent sample for analysis in this section. Since only group members are selected, not all galaxies listed in Table 1 are included in the analysis here.

In Lin et al. (2022, in preparation), images from the DECam Legacy Survey (DECaLS DR9, Dey et al. 2019) are used to derive the g - and r -band fluxes for most of the galaxies. For the few bright galaxies which have background over-subtraction problems in the DECaLS images, images from the Sloan Digital Sky Surveys (SDSS DR16, Ahumada et al. 2020) are used instead. The asymptotic fluxes are derived based on the curve of growth of fluxes. The zero-points are adjusted to convert DECaLS to SDSS magnitudes (Dey et al. 2019). Galactic extinction (Cardelli et al. 1989; Schlegel et al. 1998) is corrected. Stellar mass is estimated using the $g - r$ dependent

r -band stellar mass-to-light ratio, based on the equation from Zibetti et al. (2009).

5.1. HI Detection Rate

Although the HI detection rate is determined by the sensitivity of a survey at the distance probed, it encapsulates information on environmental effects, specifically how many galaxies survive in retaining sufficient HI gas to be detected in dense regions. However the HI detection rate can be biased by ubiquitous RFI as some galaxies with otherwise detectable HI masses are missed in RFI contaminated regions. To alleviate this problem, we conduct a completeness correction for RFI related bias. This is performed by counting the fraction of uncontaminated and thus usable channels over all the channels (χ) at a given sky position, and constructing a map of usable fractions. We show this map in the left panel of Figure 11.

In the right panel of Figure 11, we divide the group region into annuli of different projected distances from the group center. In each annulus, we count the number of galaxies detected by the FAST observation and all galaxies from the optical catalog separately. We then derive the ratio of the former type of galaxies over the latter. The final detection rate is derived by dividing this ratio by the average χ ($\bar{\chi}$) in each annulus. By doing so the uncorrected detection ratio is increased by a factor of about 1.2. From the figure we can see that the corrected HI detection rate is nearly flat outside roughly one virial radius and drops sharply toward the group center, which clearly shows the environmental stripping effects on the HI. The HI detection rate flattens at roughly 80%, which may be explained by environmental effects prior to infall galaxies fell into the main cluster/group, which refer to as pre-processing effects, internally driven evolution, or the detection threshold is not low enough.

5.2. HI-to-stellar Mass Relation

We present the HI mass fraction versus stellar mass relation of member galaxies of the NGC 4636 group in the region covered by our data. The major purpose is to understand what type of galaxies are newly detected, and to discuss their value in deepening our understanding of galaxy evolution in the group environment.

For galaxies from the optical catalog which are not detected in HI, in order to constrain their the HI-to-stellar mass relation, we derive the HI mass upper limits following Wang et al. (2021), with smoothing parameters modified according to our FAST pipeline and results. The median relation between HI mass and stellar mass from Calette et al. (2018) is used to estimate a rough HI mass. The baryonic masses can then be estimated as $1.4M_{\text{HI}} + M_*$, and the baryonic Tully–Fisher relation (McGaugh et al. 2000) is used to estimate the expected line widths. To be conservative, we calculate an upper limit to the flux integral by assuming a flux density of three times the

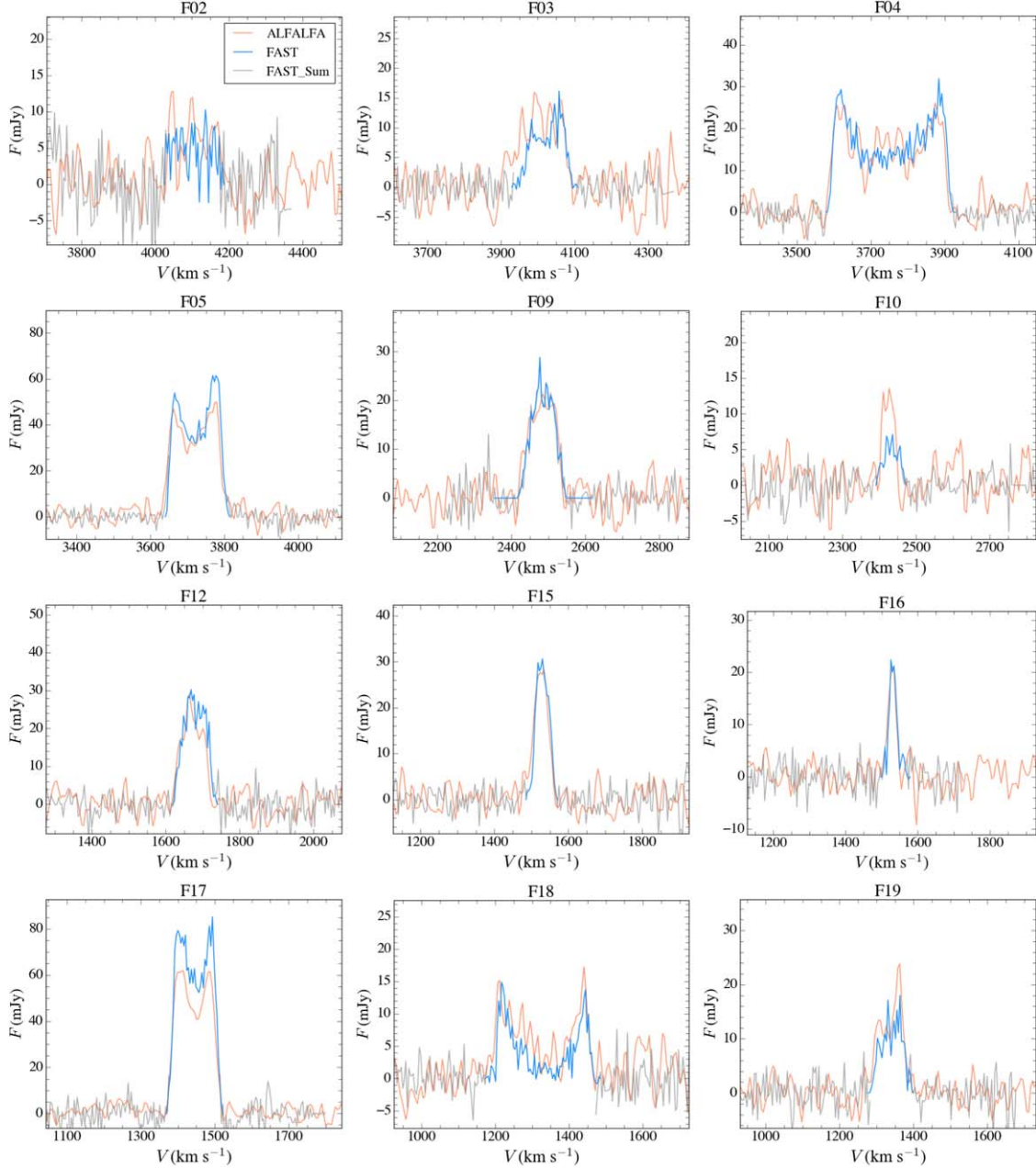


Figure 9. H I spectra of sources unresolved in the FAST observation. The spectra in blue and gray have the same meaning as in Figure 7. The spectra in orange show the ALFALFA H I data.

rms combined with the above linewidth estimate to obtain an initial guess of the upper limit of H I masses. Then the intercept of the line of upper limits as a function of stellar mass is manually shifted slightly to match the lower envelope of the real detections, to account for the fact that multi-scale smoothing has been used in source finding of SoFiA.

The relation between H I mass fraction ($f_{\text{HI}} = \frac{M_{\text{HI}}}{M_*}$) and stellar mass (M_*) for the detected H I sources in the FAST

observed region of the NGC 4636 group is presented in Figure 12. FAST lowers the detection limit by ~ 0.4 dex compared to ALFALFA, which yields three newly-detected galaxies below the H I main-sequence (galaxy No. 25, 31, 32). For the galaxies with $\log M_*/M_\odot \approx 8$, the ALFALFA detection limit is very close to the H I main-sequence, and thus the FAST data, including those upper limits, provide a better picture of H I mass distribution at such a stellar mass. Thus this

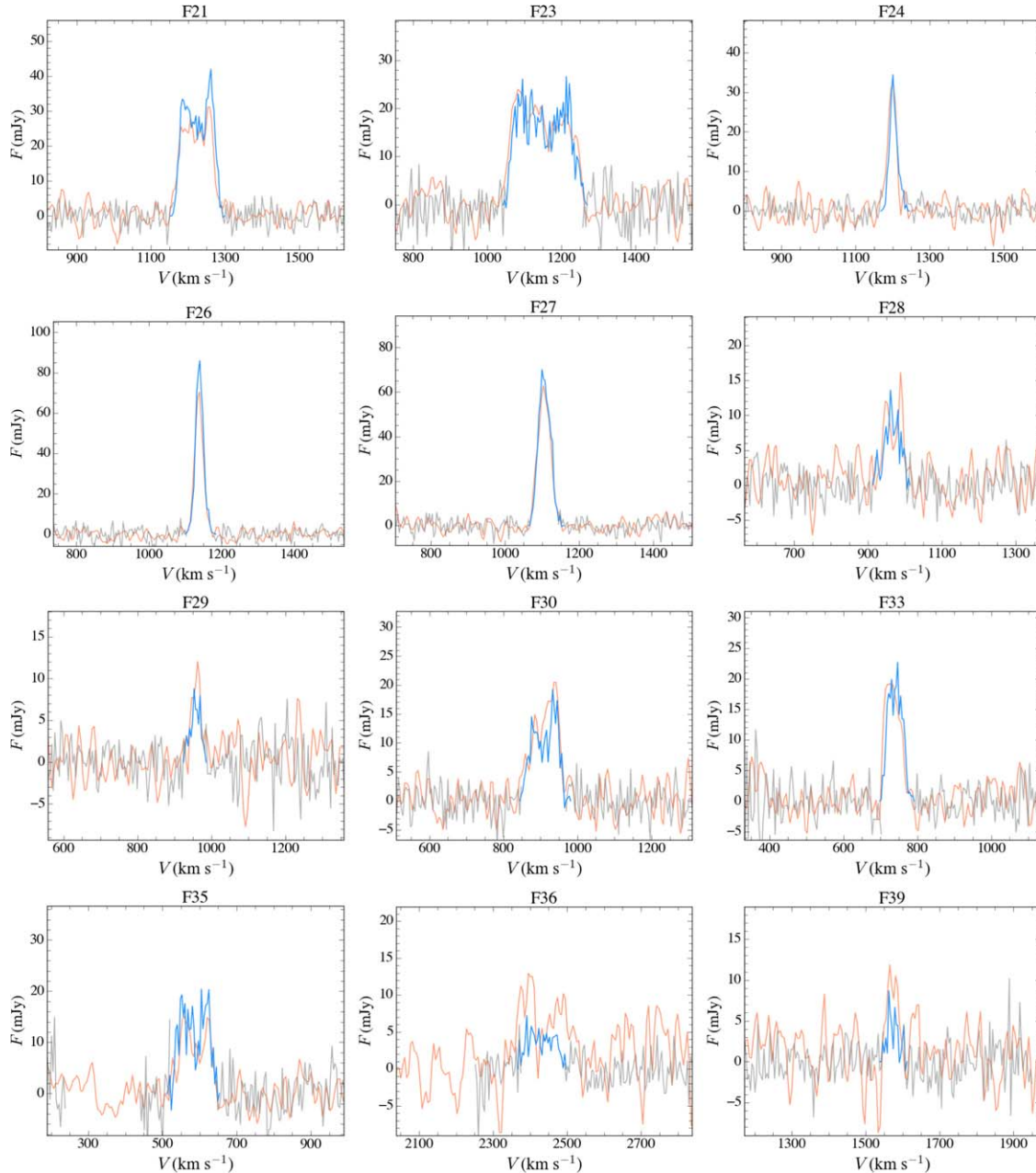


Figure 9. (Continued.)

improvement in depth provides strong support for the potential of FAST in investigating the HI poor regime of galaxies, which is particularly important for galaxies possibly experiencing fast transition in group and cluster environments.

Another new detection by FAST, No. 51_2, is far above the detection limit. It is a close pair of galaxies, which is probably the reason why it was missed by ALFALFA, as the Arecibo resolution is slightly worse. Deblending galaxies in close pairs

is important for studying galaxy evolution, because otherwise the blended HI fluxes may cause over-estimation of HI richness in related galaxies, or cause related galaxies to be rejected from the sample resulting in selection biases.

6. Resolved Interacting Candidate Systems

We detect four potentially interacting systems which are clearly more extended than the beam FWHM. Among them,

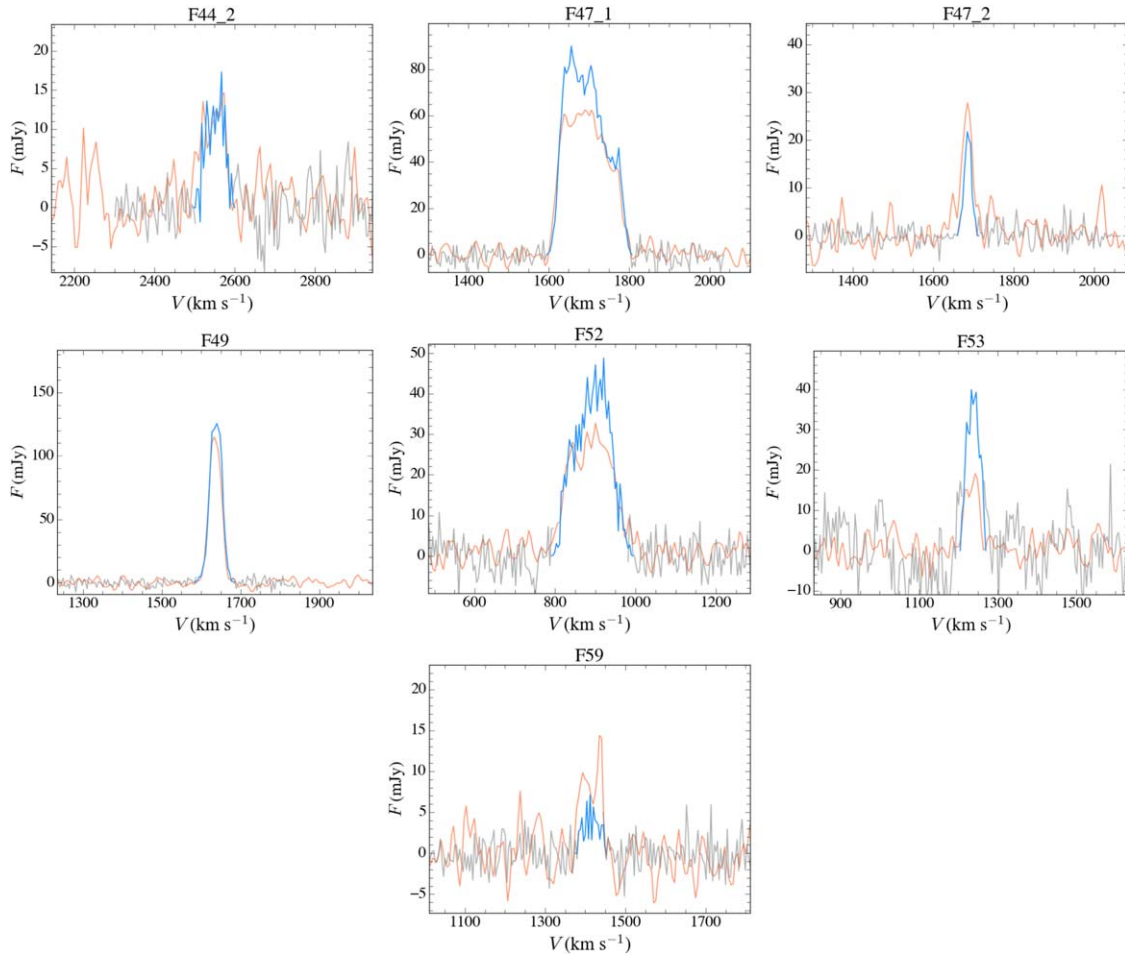


Figure 9. (Continued.)

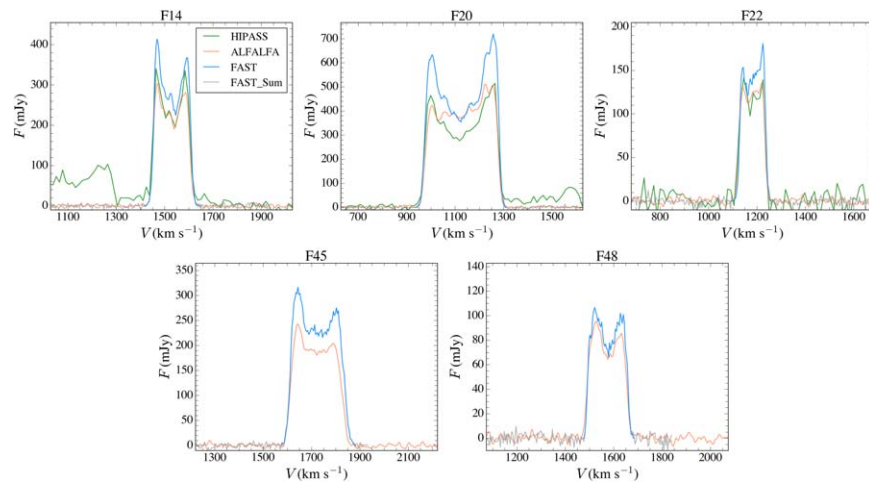


Figure 10. H I spectra of sources resolved in the FAST observation. The spectra in blue, gray, and orange have the same meaning as in Figure 9. The spectra in green show HIPASS data.

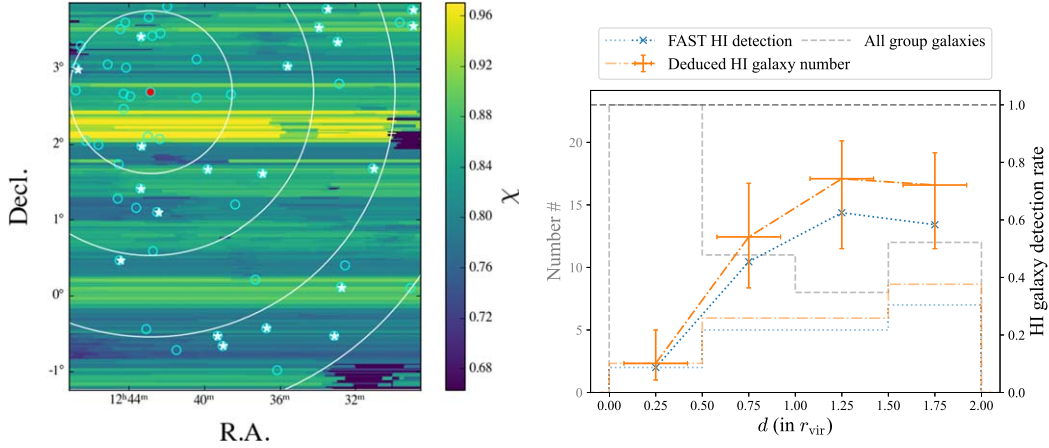


Figure 11. Usable channel number fraction map for the NGC 4636 FAST data (left) and the source distribution and HI detection rate (right). On the left panel, the red dot marks the center of the NGC 4636 group. The sky positions of FAST HI detected members, and of the galaxies in the optical sample are shown by cyan stars and cyan circles respectively. The white circles correspond to 0.5, 1, 1.5, and 2 times the virial radius. On the right panel, the gray and blue histograms show the number counts of group members as a function of projected group centric radius for the optical sample, and for the FAST HI detected sample, respectively. The blue line shows the uncorrected HI detection rate, which is the blue histogram divided by the gray histogram. The RFI corrected version of the HI detection number counts and the detection rate are in orange histograms and orange lines respectively. The error bars are derived from the standard deviation of the detection rate and virial radius of each annuli.

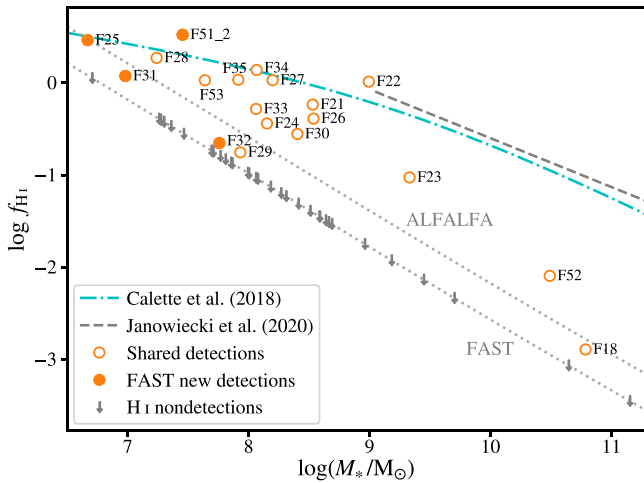


Figure 12. Relation between HI gas fraction ($f_{\text{HI}} = \frac{M_{\text{HI}}}{M_*}$) and stellar mass (M_*) for galaxies detected by FAST in the NGC 4636 group. Galaxies detected in HI in the FAST observing region but not identified as members of the NGC 4636 group are not plotted. Orange circles are galaxies detected by FAST, with filled ones being a new detections by FAST. HI masses are calculated from FAST data where possible. Grey dotted lines are estimated HI detection upper limits for this FAST survey (lower line) and ALFALFA (upper line). HI non-detections of a previously selected optical sample in the same region are marked by gray arrows, showing the upper limit of HI masses. Cyan dotted-dashed line and gray dashed lines are the median relation of late-type galaxies (Calette et al. 2018), and massive star-forming galaxies (Janowiecki et al. 2020), respectively.

three are paired galaxies, and the remaining one is a triplet system. We present their optical images with HI moment maps in Figure 13. These images are not as well resolved as can be achieved by interferometric observations, but they possibly

capture fainter fluxes, and are thus more sensitive to features like the tidally interacting tails between galaxies. On the other hand, if no tidal tails or bridges are detected in the HI, then the interaction is likely to be weak or at an early stage. They can be combined with interferometric images in the future. We discuss more details of these resolved systems below.

6.1. NGC 4517/4517A

NGC 4517 (FAST J123245+000645, F20) is a spiral edge-on galaxy which has a companion NGC 4517A (FAST J123228+002321, F14) located $\sim 18'$ (110 kpc) away in a north-western direction (Figure 13). Their velocity ranges do not overlap with each other, and the difference between their HI central velocities is $\sim 400 \text{ km s}^{-1}$ (Figure 14). Figure 13 shows no obvious HI gas interaction between them and the lowest contour of HI intensity extends toward NGC 4517. Neumayer et al. (2011) found that NGC 4517A has a large offset between the galaxy nucleus and the kinematic center of $\text{H}\alpha$ and demonstrated that the potential nuclear starburst can affect the central velocity field. As the stellar mass of NGC 4517 ($\log M^*/M_\odot = 10.4$) is much more massive than its dwarf companion ($\log M^*/M_\odot = 6.7$), this feature can also be caused by the tidal effect from the more massive galaxy of this system.

Meanwhile, NGC 4517 shows consistency of central peaks between optical and HI map. The deep r -band imaging from Mosenkov et al. (2020) shows that the outer shape of NGC 4517 is oval and no obvious tidal disturbance is visible. Nevertheless, the higher spatial resolution of HI emission of ASKAP reveals that NGC 4517 has a clockwise warp-like structure in its asymmetric HI gas distribution (Figure 5 in Lee et al., submitted), which is relatively consistent with the lowest

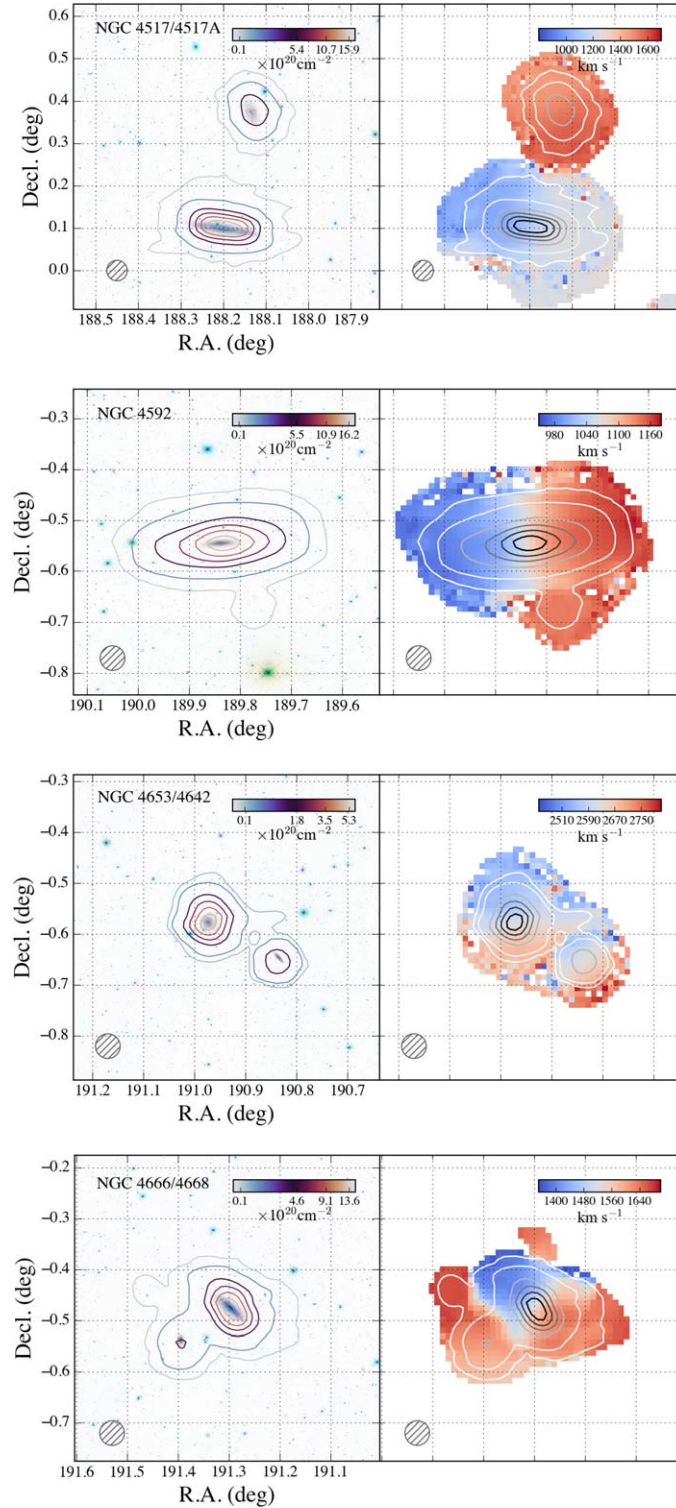


Figure 13. The optical and H I images of four spatially resolved sources with potential tidal interaction activities. The four galaxy systems are NGC 4517/4517A, NGC 4592, NGC 4653/4642, and NGC 4666/4668, from top to bottom, and their maximum values of 0th moment are 17.47 , 17.80 , 5.79 , and $14.92 \times 10^{20} \text{ cm}^{-2}$, respectively. Left: The inverse SDSS RGB image overlaid with contours of H I moment zero map. The lowest level of colored contours is $0.1 \times 10^{20} \text{ cm}^{-2}$, and then from 5% to 85% with 20% intervals of maximum value. The shaded circle on left corner is the FAST beam FWHM. Right: The 1st moment map of H I overlaid with similar contours in left image.

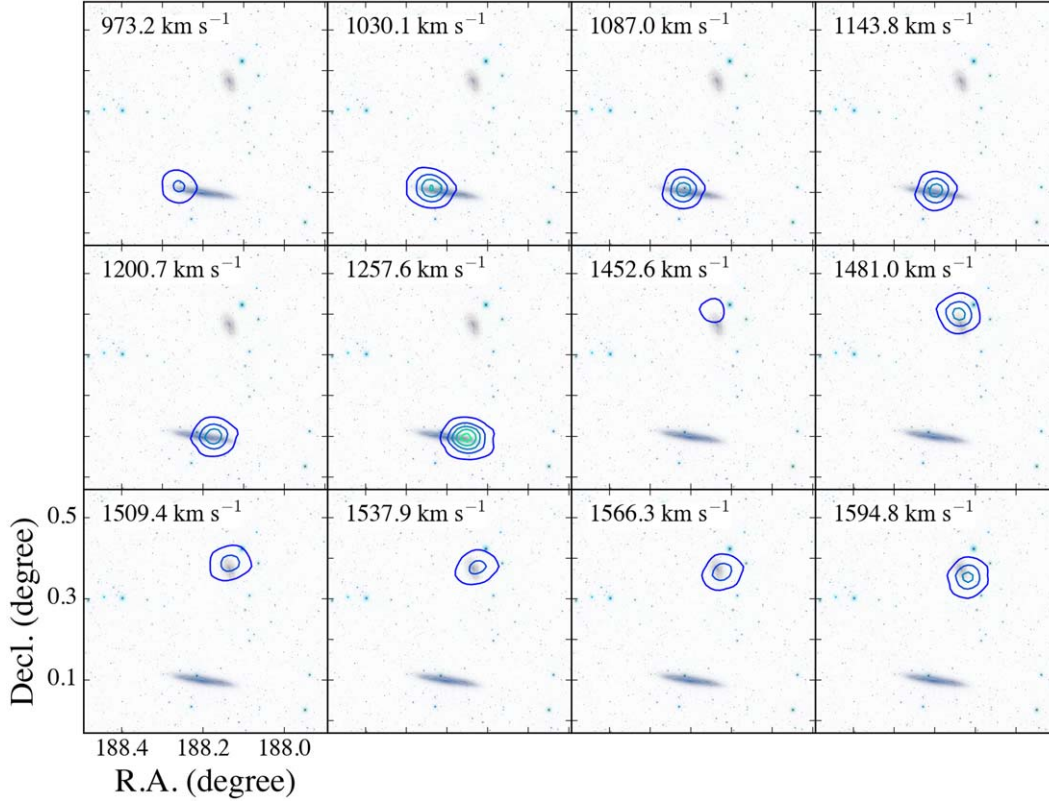


Figure 14. The H I channel maps of NGC 4517/4517A. The contours of H I flux intensity are ranging 8%–88% (the lowest level is 3σ as the rms is ~ 0.01 Jy beam $^{-1}$) with interval of 20% of maximum value of 0.41 Jy beam $^{-1}$, overlaid with optical image and the velocity range is 973.2–1257.6 km s $^{-1}$, with intervals of 56.9 km s $^{-1}$ for panels 1–6, and 1452.6–1594.8 km s $^{-1}$, with intervals of 28.4 km s $^{-1}$ for panels 7–12, corresponding to 14 channels and seven channels, respectively.

contour of H I intensity in Figure 13. Karachentsev et al. (2014) and Kim et al. (2020) derived accurate distances for NGC 4517 and potential group members, and concluded that this galaxy is located in front of Virgo cluster and is infalling toward the cluster. Thus, this system can be a prototype of tidally driven preprocessing for the Virgo galaxy population. In summary, although NGC 4517 has no obvious bridges or tails in H I linking with its companion NGC 4517A, they possibly interacting at an early stage or having a distant (maybe fly-by) interaction.

6.2. NGC 4592

NGC 4592 (FAST J123918–003155, F51_1) is a spiral galaxy with a faint companion galaxy (FAST J123903–003951, F51_2) located to the south west (Figure 13). The H I gas of the NGC 4592 largely extends out of its optical disk and the Compared with the optical image, the contours of the H I intensity map of the bigger galaxy in this system displace toward to the southern side, while the smaller companion has a radial velocity smoothly transitioning to the receding side of the disk of the bigger galaxy (Figure 15, ~ 1143.6 km s $^{-1}$). Kim et al. (2020) derive the distance of NGC 4592 and NGC 4517

to be 9.28 Mpc and 9.07 Mpc, respectively, so they are spatially adjacent to each other. They also stated that there are other five nearby dwarf galaxies with similar distances, and concluded that they together form the NGC 4517 group. Potential association of the H I with the dwarf satellites suggests that this system is likely in the intermediate or late stage of merging with FAST J123903–003951, and may be perturbed by more dwarf satellite galaxies either not detected or not de-blended from our data.

6.3. NGC 4653/4642

NGC 4653 (FAST J124350–003341, F43_1) and NGC 4642 (FAST J124318–003832, F43_2) comprise a paired galaxy with projected separation of ~ 50 kpc and with H I spectra which overlap in velocity range (Figure 13). Optically, NGC 4653 is a face-on galaxy and both its optical and H I gas is asymmetric and extend toward its edge-on companion, NGC 4642. The contours of H I intensity in Figure 13 show a tidal tail reaching out of the western arm of NGC 4653, indicating perturbation from tidal interactions. It has weak but obvious outer disturbances in its H I distribution in Figure 16. The gas in the western arm stretches toward

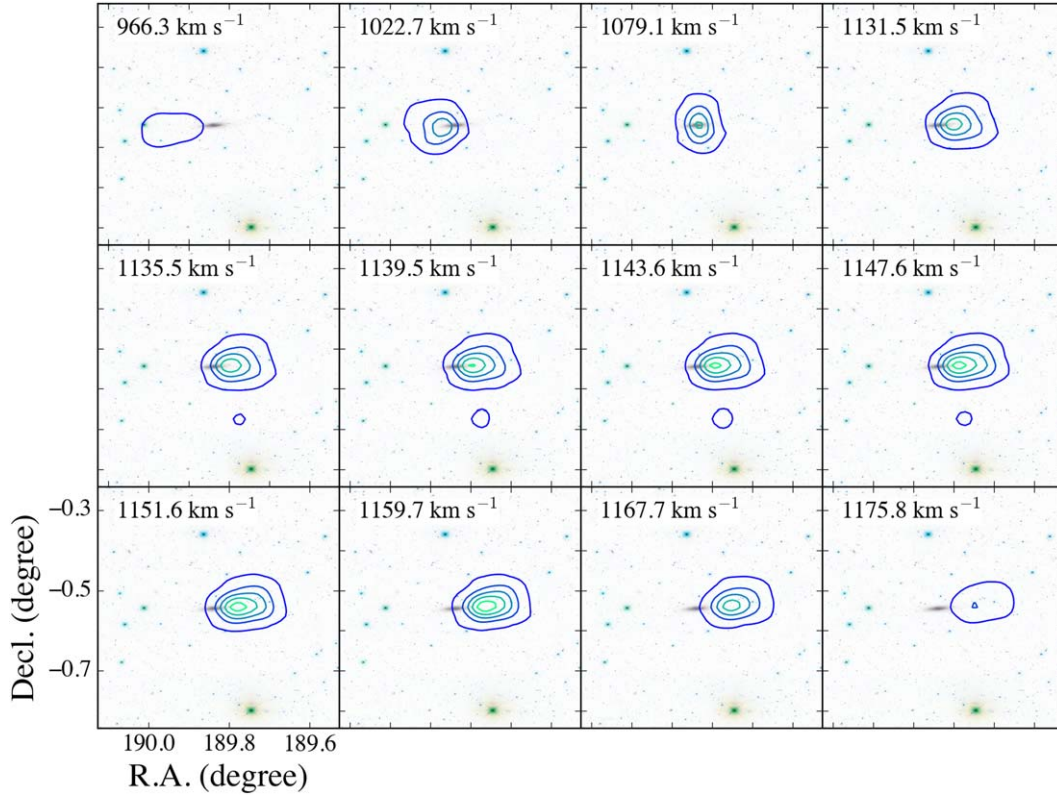


Figure 15. The H I channel map of NGC 4592. The contours of H I flux intensity are ranging from 5% to 85% (the lowest level is 2σ as the rms is $\sim 0.02 \text{ Jy beam}^{-1}$) with interval of 20% of maximum value of $0.64 \text{ Jy beam}^{-1}$, overlaid with optical image and the velocity range is $966.3\text{--}1175.8 \text{ km s}^{-1}$, with intervals of 56.4 km s^{-1} for panel 1–3, 4.1 km s^{-1} for panels 4–9, and 8.1 km s^{-1} for panels 10–12, corresponding to 14, one, and two channels, respectively. The velocity of NGC 4592’s companion (51_2) is $\sim 1141 \text{ km s}^{-1}$, as shown from panels 5–8.

NGC 4642 with increasing velocity. Although there is no prominent HI gas bridge connecting these two galaxies, the possibility of a merger in the near future is high. These two galaxies may be at a relatively early stage of tidal interaction and merger.

6.4. NGC 4666/4668

NGC 4666 (FAST J124508–002750, F50_1), NGC 4668 (FAST J124532–003203, F50_2), and two dwarf galaxies constitute a galaxy group beyond the Virgo cluster (Walter et al. 2004). We detect significant HI emission from NGC 4666, NGC 4668, and FAST J124548–002554 (F50_3), but unlike Walter et al. (2004), we do not identify the individual signal of another dwarf galaxy, VLA J124445.6–002536. We cannot deblend this source from the data cube because it mixes with the extended HI emission of NGC 4666 and the projected separation between them is ~ 4.5 . The 0th and 1st moment maps and channel maps of HI in Figures 13 and 17 show that the HI gas between three galaxies are experiencing interactions with each other. Based on the VLA HI images with much higher spatial resolution, Walter et al. (2004) provided clear evidence that

NGC 4666 is interacting with NGC 4668 and FAST J124547–002603. NGC 4666 is surrounded by prominent tidal arms while there is also an HI bridge between NGC 4668 and VLA J124547.9–002556 (FAST J124547–002603). Meanwhile, this interaction may have caused the starburst activity in the center of NGC 4666 (Walter et al. 2004). Walter et al. (2004) and Lee et al. (submitted) both detected CO emission in NGC 4666 with a high surface density in the central region. The distribution and velocity of CO gas is similar to the HI gas and trace rotation of central part of the disk. Since the distributions of HI gas from interferometric (VLA, ASKAP, Lee et al. submitted) and single-dish observations show extended and disturbed features, it is more evidence that NGC 4666 is under strong gravitational interaction with its neighbor galaxies. In conclusion, the galaxies in this group are close encounters and their gas kinematics are experiencing strong perturbations.

7. Summary

In this work, we have mapped a $5^\circ \times 5^\circ$ region of the NGC 4636 galaxy group with 21 cm HI emission using FAST. With reasonable success, we have solved several problems met in this unique “shared risk” stage of the telescope, including

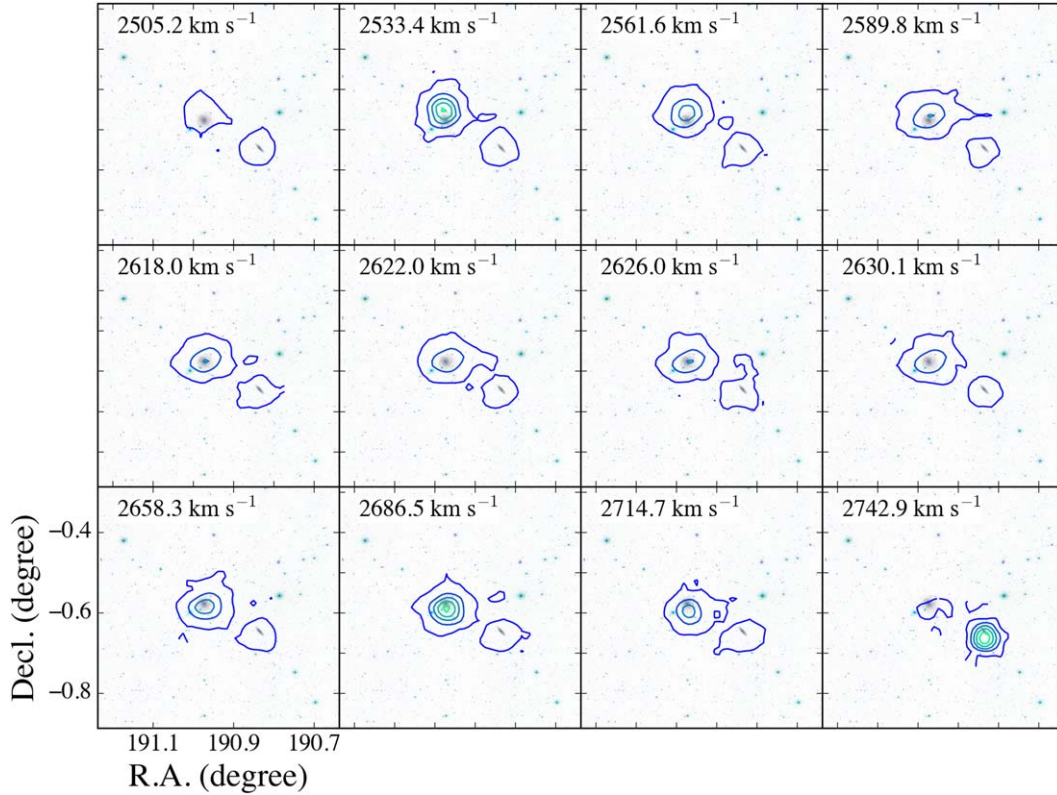


Figure 16. The channel map of NGC 4653/4642. The contours of HI flux intensity are ranging from 3% to 83% (the lowest level is 2σ as the rms is $\sim 0.003 \text{ Jy beam}^{-1}$) with interval of 20% of maximum value of $0.15 \text{ Jy beam}^{-1}$, overlaid with optical image and the velocity range is $2505.2\text{--}2742.9 \text{ km s}^{-1}$, with intervals of 28.2 km s^{-1} for panels 1–4, 4.1 km s^{-1} for panels 5–8, and 28.2 km s^{-1} for panels 9–12, corresponding to seven, one and seven channels, respectively.

unsynchronized noise-diode injection and frequent RFI contamination. We have developed a pipeline to process FAST HI data following standard procedure of data reduction for drift scan surveys like HIPASS. The source finding procedure was conducted by combining visual inspection with the standard software SoFiA. We detected 73 sources in the NGC 4636 region in total. Eight of them are partly contaminated by RFI in the FAST data and had to be excluded from the most of the analysis (all the items below except for item 1). The analysis reveals the following results.

1. In the mutual sky region covered by both our observation and ALFALFA, we detect practically all the sources, except for one where the data is fully masked due to RFI contamination.
2. For the 36 clearly-detected sources in common with ALFALFA, except for the fluxes lower than $\sim 1 \text{ Jy km s}^{-1}$, the data show consistent integral HI fluxes and spectra where the HI disks are unresolved by the FAST and ALFALFA beams. For resolved sources, our source finding strategy appears better at capturing extended emission.
3. There are 24 newly detected galaxies. Among the new detections, 14 sources are beyond the sky coverage of

ALFALFA, and the remaining 10 sources with the corresponding optical counterparts are in the mutual sky but newly detected due to the lower detection limit and slightly smaller beam size of FAST. Thus the FAST observation expands the previous HI catalog based on ALFALFA by at least 20% (10 out of 47).

4. In the NGC 4636 group, the HI detection rate rises from less than 10% near the group center to nearly 75% beyond the virial radius, and then flattens. FAST lowers the detection limit of HI masses by ~ 0.4 dex compared to ALFALFA, allowing us to study the HI poor population at a stellar mass of $10^8 M_{\odot}$.
5. The FAST data resolved four galaxy systems potentially undergoing tidal interactions. The asymmetry of HI distribution and the HI bridge between galaxies provide evidence for the systems to be genuinely interacting, and gives clues about the interacting stage of the systems.

In conclusion, FAST has a unique capability for detecting HI-poor galaxies, and will be especially important for studying galaxies likely undergoing fast transition between the HI rich and HI poor regimes in dense environments. Combined with the interferometric data from ASKAP, a detailed analysis of galaxy

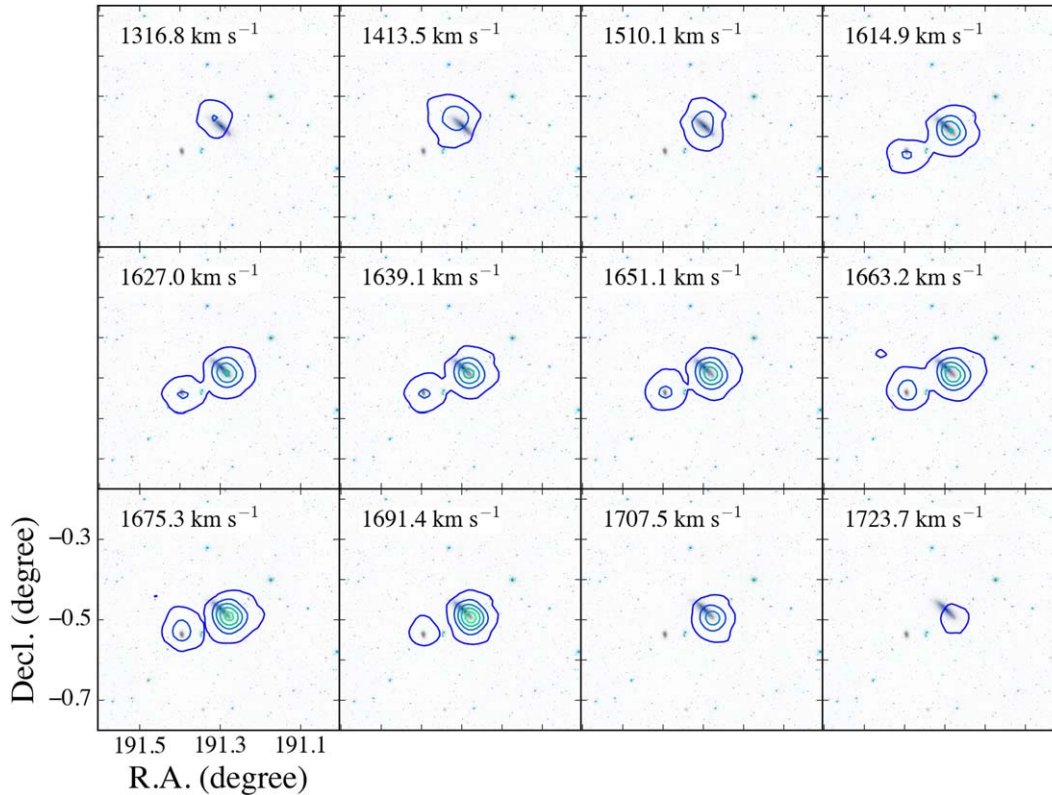


Figure 17. The channel map of NGC 4666/4668. The contours of H I flux intensity are ranging from 5% to 85% (the lowest level is 2σ as the rms is ~ 0.007 Jy beam $^{-1}$) with interval of 20% of maximum value of 0.25 Jy beam $^{-1}$, overlaid with optical image and the velocity range is 1316.8–1719.6 km s $^{-1}$, with intervals of 96.7 km s $^{-1}$ for panels 1–3, 12.1 km s $^{-1}$ for panels 4–9, and 16.1 km s $^{-1}$ for panels 10–12, corresponding to 24, three, and four channels, respectively.

evolution in the NGC 4636 group will be presented in our next work in the near future (Lin et al. 2022, in preparation).

Acknowledgments

We thank the anonymous referee for the helpful comments and suggestions that improved the paper. This work was supported by the National Natural Science Foundation of China (11988101, 11721303, 11991052, 12011540375, 12073002, and 11903003) and the China Manned Space Project (CMS-CSST-2021-A04, CMS-CSST-2021-A06). J.W. thanks support from the science research grants from the China Manned Space Project with No. CMS-CSST-2021-B02. Parts of this research were conducted by the Australian Research Council Centre of Excellence for All Sky Astrophysics in 3 Dimensions (ASTRO 3D), through project No. CE170100013. K.S. acknowledges support from the Natural Sciences and Engineering Research Council of Canada (NSERC). We used data from FAST (Five-hundred-meter Aperture Spherical radio Telescope), a Chinese national mega-science facility operated by National Astronomical Observatories, Chinese Academy of Sciences. We thank Hongwei Xi, Zheng Zheng, Ningyu Tang, Xuanyi Lyu for useful advice and discussion.

ORCID iDs

Xuchen Lin  <https://orcid.org/0000-0002-4250-2709>
Bumhyun Lee  <https://orcid.org/0000-0002-3810-1806>

References

- Ahoranta, J., Finoguenov, A., Pinto, C., et al. 2016, *A&A*, **592**, A145
 Ahumada, R., Prieto, C. A., Almeida, A., et al. 2020, *ApJS*, **249**, 3
 Auld, R., Minchin, R. F., Davies, J. I., et al. 2006, *MNRAS*, **371**, 1617
 Baldi, A., Forman, W., Jones, C., et al. 2009, *ApJ*, **707**, 1034
 Barnes, D. G., Staveley-Smith, L., de Blok, W. J. G., et al. 2001, *MNRAS*, **322**, 486
 Blanton, M. R., & Moustakas, J. 2009, *ARA&A*, **47**, 159
 Brown, T., Catinella, B., Cortese, L., et al. 2017, *MNRAS*, **466**, 1275
 Calette, A. R., Avila-Reese, V., Rodríguez-Puebla, A., Hernández-Toledo, H., & Papastergis, E. 2018, *RMxAA*, **54**, 443
 Cardelli, J. A., Clayton, G. C., & Mathis, J. S. 1989, *ApJ*, **345**, 245
 Catinella, B., Saintonge, A., Janowiecki, S., et al. 2018, *MNRAS*, **476**, 875
 Condon, J. J., Cotton, W. D., Greisen, E. W., et al. 1998, *AJ*, **115**, 1693
 Cortese, L., Catinella, B., & Smith, R. 2021, *PASA*, **38**, e035
 Dey, A., Schlegel, D. J., Lang, D., et al. 2019, *AJ*, **157**, 168
 Evrard, A. E., Bialek, J., Busha, M., et al. 2008, *ApJ*, **672**, 122
 Giovanelli, R., Haynes, M. P., Kent, B. R., et al. 2005, *AJ*, **130**, 2598
 Haynes, M. P., Giovanelli, R., Martin, A. M., et al. 2011, *AJ*, **142**, 170
 Haynes, M. P., Giovanelli, R., Kent, B. R., et al. 2018, *ApJ*, **861**, 49
 Hoffman, G. L., Dowell, J., Haynes, M. P., & Giovanelli, R. 2019, *AJ*, **157**, 194

- Janowiecki, S., Catinella, B., Cortese, L., Saintonge, A., & Wang, J. 2020, *MNRAS*, **493**, 1982
- Jiang, P., Yue, Y., Gan, H., et al. 2019, *SCPMA*, **62**, 959502
- Jiang, P., Tang, N.-Y., Hou, L.-G., et al. 2020, *RAA*, **20**, 064
- Karachentsev, I. D., Tully, R. B., Wu, P.-F., Shaya, E. J., & Dolphin, A. E. 2014, *ApJ*, **782**, 4
- Kilborn, V. A., Forbes, D. A., Barnes, D. G., et al. 2009, *MNRAS*, **400**, 1962
- Kim, Y. J., Kang, J., Lee, M. G., & Jang, I. S. 2020, *ApJ*, **905**, 104
- Koribalski, B. S., Staveley-Smith, L., Kilborn, V. A., et al. 2004, *AJ*, **128**, 16
- Koribalski, B. S., Staveley-Smith, L., Westmeier, T., et al. 2020, *Ap&SS*, **365**, 118
- Kourkchi, E., & Tully, R. B. 2017, *ApJ*, **843**, 16
- McGaugh, S. S., Schombert, J. M., Bothun, G. D., & de Blok, W. J. G. 2000, *ApJL*, **533**, L99
- Meyer, M. J., Zwaan, M. A., Webster, R. L., et al. 2004, *MNRAS*, **350**, 1195
- Mosenkov, A., Rich, R. M., Koch, A., et al. 2020, *MNRAS*, **494**, 1751
- Neumayer, N., Walcher, C. J., Andersen, D., et al. 2011, *MNRAS*, **413**, 1875
- Reiprich, T. H., & Böhringer, H. 2002, *ApJ*, **567**, 716
- Schlegel, D. J., Finkbeiner, D. P., & Davis, M. 1998, *ApJ*, **500**, 525
- Serra, P., Koribalski, B., Kilborn, V., et al. 2015, *MNRAS*, **452**, 2680
- Serra, P., Westmeier, T., Giese, N., et al. 2015, *MNRAS*, **448**, 1922
- Walter, F., Dahlem, M., & Lisenfeld, U. 2004, *ApJ*, **606**, 258
- Wang, J., Koribalski, B. S., Serra, P., et al. 2016, *MNRAS*, **460**, 2143
- Wang, J., Staveley-Smith, L., Westmeier, T., et al. 2021, *ApJ*, **915**, 70
- Westmeier, T., Kitaeff, S., Pallot, D., et al. 2021, *MNRAS*, **506**, 3962
- Winkel, B., Lenz, D., & Flöer, L. 2016, *A&A*, **591**, A12
- Zibetti, S., Charlot, S., & Rix, H.-W. 2009, *MNRAS*, **400**, 1181